

Qingming Chang · J. I. D. Alexander

## Analysis of single droplet dynamics on striped surface domains using a lattice Boltzmann method

Received: 25 August 2005 / Accepted: 5 December 2005 / Published online: 3 February 2006  
© Springer-Verlag 2006

**Abstract** In this paper, the behavior of a micron-scale fluid droplet on a heterogeneous surface is investigated using a two-phase lattice Boltzmann method (LBM). The two-phase LBM permits the simulation of the time dependent three-dimensional motion of a liquid droplet on solid surface patterned with hydrophobic and hydrophilic strips. A nearest-neighbor molecular interaction force is used to model the adhesive forces between the fluid and solid walls. The solid heterogeneous wall is a uniform hydrophilic substrate painted with hydrophobic strips. The model is validated by demonstrating the consistency of the simulation results with an exact solution for capillary rise and through qualitative comparison of computed dynamic contact line behavior with experimentally measured surface properties and observed surface shapes of a droplet on a heterogeneous surface. The dependence of spreading behavior on wettability, the width of hydrophobic strip, initial location of the droplet relative to the strips, and gravity is investigated. A decrease in contact angle of the liquid on a hydrophilic surface may lead to breakup of the droplet for certain substrate patterns. The simulations suggest that the present lattice Boltzmann (LB) model can be used as a reliable way to study fluidic control on heterogeneous surfaces and other wetting related subjects.

**Keywords** Fluid droplet · Lattice Boltzmann method · Heterogeneous surface · Nearest-neighbor molecular interaction force · Wetting and spreading

### 1 Introduction

Liquid droplet spreading on surfaces occurs in many industrial processes, such as painting and coating, inkjet printing, lubrication, and gluing. A large number of experimental, theoretical, and numerical studies on liquid droplet spreading have been performed (Pasandideh-Fard et al. 1996; De Gennes 1985; Trevino et al. 1998). As a result, the physics of liquid droplet behavior on flat homogeneous surfaces is relatively well understood. In contrast, motivated largely by growing interest in ‘microfluidics’, fluid behavior on small scale heterogeneous surfaces is not as well characterized and is currently the subject of widespread investigation. Of particular interest is the control of liquid movement, mass flow rates and residence times in microchannels and ducts and on physically and chemically patterned substrates. The range of possible surface configurations and the underlying complexity of the processes (De Coninck 2001) make the simulation of these processes challenging. The complexity arises from the chemistry of the solid surface, contamination of the liquid surface, solid surface roughness and dissolved components in the liquid (e.g., surfactants and polymers) (Blake 1993). The wetting of heterogeneous surface exhibits several unusual features that have been recently brought to light through studies of structured surfaces (Lenz and Lipowsky 1998). For example, such systems can undergo morphological transitions in which the wetting phase experiences an abrupt change in shape (Gau et al. 1999).

In many processes, for example, printing, droplets typically have length scales of microns. Experimental work on micro and mesoscopic droplets can be difficult because of the length- and time-scales involved. The ability to predict droplet behavior as a function of surface chemistry and liquid properties using numerical modeling is an attractive option both for a parametric investigation of the physical behavior and for design

Qingming Chang (✉) · J. I. D. Alexander  
National Center for Space Exploration Research,  
Department of Mechanical and Aerospace Engineering,  
Case Western Reserve University, 10900 Euclid Avenue,  
Cleveland, OH 44106, USA  
E-mail: qxc3@case.edu  
Tel.: +1-216-3680530  
Fax: +1-216-3686445

and interpretation of experiments. One useful modeling tool is molecular dynamics (MD). In earlier work, MD simulations have been carried out to study the spreading of sessile drops on flat homogeneous surfaces (D'Ortona et al. 1996; Bekink et al. 1996; Hataja et al. 1996; de Ruijter et al. 1999), flat heterogeneous surfaces (Adão et al. 1999), and porous surfaces (Deng et al. 2002). MD simulations yield molecular level information on the influence of surface structure and chemistry on the wetting and spreading behavior. Because of computational overhead and the restriction to two or three body potentials, however, such MD simulations are unable to access a wide range of system parameters (e.g., size and distribution of physical and chemical heterogeneities of substrates, interfacial tension and viscosity of fluids, and gravity) that can influence mesoscopic behavior.

In this paper, the specific aim is to model the behavior of a droplet on a chemically heterogeneous substrate by employing a modified LBM. The LBM is a convenient simulation tool to solve multiphase fluid dynamics problems on a variety of length scales. Its appeal is that, in contrast to traditional CFD methods that solve macroscopic equations, the LBM simulates fluid flow based on a microscopic model or mesoscopic kinetic equations. This intrinsic feature is attractive to those who wish to incorporate microscopic or mesoscopic features and processes that are either not used, or are difficult to incorporate, in traditional CFD simulation models. In particular, the dynamics of multiple fluids interfaces is often difficult to simulate by traditional approaches but can be modeled effectively by LBM accounting for molecular interactions near an interface (He et al. 1999; Shan and Chen 1993; Succi 2001).

There are several different multiphase LB models currently in use. The first multiphase fluid LBM was Chromodynamic model proposed by Gunstensen et al. (1991) and modified by Grunau et al. (1993). In this model, 'red' and 'blue' particle distribution functions were introduced to mimic two different fluids. The main drawback of this model is that the 'recoloring' process results in artificial anisotropic surface tension and induces unphysical currents near the interfaces. The pseudopotential model (Shan and Chen 1993, 1994) avoids artificial 'recoloring' process by introducing an additional force term explicitly to the velocity field, and thus has been quite successful in simulation of several fundamental interfacial phenomena. However, the choice of the force term ignores the effect of the repulsive core and leads to a 'mass collapse' phenomenon in which particle density approaches infinity. Although this 'black-hole' problem can be reduced by modifying the force term, this leads to a thermodynamic inconsistency (He and Doolen 2002), and limits its application in multiphase thermodynamics. Swift et al. (1995, 1996) developed a model for multiphase fluids using the concepts of free-energy functional. Compared with pseudopotential

model, the free-energy model is fully consistent with Maxwell's equal-area construction, especially for low-temperature conditions. Furthermore, since the free-energy model admits local momentum conservation, the interfacial spurious velocity is nearly eliminated. Dupuis and Yeomans (2004), Dupuis et al. (2005b), and Leopoldes et al. (2003) have applied this free-energy based LBM to dynamic analysis of a droplet spreading on a solid surface.

In this paper, we adopt a three-dimensional, two-phase LBM based on effective molecular interaction force, which was recently developed by He et al. (1998). The adhesive force of the solid surface proposed by Martys (1996) is used to model the wetting phenomenon. The advantage of this approach for wetting problems is that it allows us to tune equilibrium thermodynamic properties such as the surface tension or static contact angle by matching LBM solutions with analytic predictions of interface shapes for known surface tension values and static wetting angles. Thus, the equilibrium wetting properties of the substrate can be readily defined and controlled, and the dynamic properties are determined by the nature of the interfacial molecular interaction model that is employed. The model is checked by showing the consistency of the theoretical solution with the simulation results of capillary rise and by comparing the measured dynamic contact line with experimentally measured surface properties of a droplet on a multi-stripped heterogeneous surface. The effects of some parameters on the droplet spreading are then analyzed.

---

## 2 Numerical model

### 2.1 The continuous Boltzmann model

The LBM has evolved from the lattice-gas automata (LGA) model (Frisch et al. 1987; Rothman and Zaleski 1994), and as such is often referred to as a mesoscopic approach (in contrast to, say, the more traditional continuum mechanical formulations). Different from LGA, which is a direct consequence of the single particle Boolean operation and thus suffers a problem of the statistical noise in the computed hydrodynamic fields, the LBM employs real-valued densities of microscopic particles that move along each bond of the lattice, following the motion of a distribution of microscopic particles. The key idea is to solve a discretized Boltzmann equation on a regular lattice, where the fluid is modeled with a particle distribution function. The density distribution function represents the mass of fluid 'particles' at a location  $\mathbf{r}$  with mass  $m$  moving with a given velocity  $\mathbf{e}$  per unit volume of phase space. The dimension of the distribution function is mass per unit volume of  $\mathbf{r} - \mathbf{e}$  space (or phase space). The distribution function satisfies the Boltzmann equation (Chapman and Cowling 1970). That is

$$\partial_t f(\mathbf{r}, \mathbf{e}, t) + \mathbf{e} \cdot \nabla_{\mathbf{r}} f(\mathbf{r}, \mathbf{e}, t) + \mathbf{a} \cdot \nabla_{\mathbf{e}} f(\mathbf{r}, \mathbf{e}, t) = \Omega(f), \quad (1)$$

where  $\nabla_{\mathbf{e}} = \frac{\partial}{\partial \mathbf{e}}$ ,  $\nabla_{\mathbf{r}} = \frac{\partial}{\partial \mathbf{r}}$ , and  $\mathbf{a} = \frac{d\mathbf{e}}{dt}$  and occurs when a force such as gravity or magnetic field is acting on the fluid particles.

To obtain a tractable solution it is necessary to specify the form of the collision operator in a simple enough way that a solution is possible, but the essential physics is retained. Two major assumptions are made for simplification of the collision term. The first assumption is that only binary collisions are taken into account. The second assumption is that the velocity of a molecule is uncorrelated with its position. Under these assumptions the collision term is expressed in the form known as the ‘BGK’ collision operator (Bhatnagar et al. 1954), which has proved useful for certain applications. That is

$$\Omega = -\frac{f - f^{\text{eq}}}{\tau}, \quad (2)$$

where  $\tau$  is the relaxation time,  $f^{\text{eq}}$  is the local equilibrium distribution function given by (Chapman and Cowling 1970; Cercignani 1975)

$$f^{\text{eq}} = \frac{\rho}{(2\pi RT)^{D/2}} \exp\left[-\frac{(\mathbf{e} - \mathbf{u})^2}{2RT}\right]. \quad (3)$$

Here  $D$ ,  $R$ ,  $T$ ,  $\rho$ ,  $\mathbf{u}$  are the spatial dimension, gas constant, macroscopic temperature, density and macroscopic velocity, respectively. The single phase Boltzmann-BGK equation then takes the form:

$$\partial_t f(\mathbf{r}, \mathbf{e}, t) + \mathbf{e} \cdot \nabla_{\mathbf{r}} f(\mathbf{r}, \mathbf{e}, t) + \mathbf{a} \cdot \nabla_{\mathbf{e}} f(\mathbf{r}, \mathbf{e}, t) = -\frac{f - f^{\text{eq}}}{\tau}. \quad (4)$$

The third term on the left-hand side of Eq. 4 is approximated by assuming that  $f - f^{\text{eq}}$  is small enough that the derivative  $\nabla_{\mathbf{e}} f$  in the force term can be approximated as (He et al. 1998)

$$\nabla_{\mathbf{e}} f \approx \nabla_{\mathbf{e}} f^{\text{eq}} = -\frac{\mathbf{e} - \mathbf{u}}{RT} f^{\text{eq}}. \quad (5)$$

Substitution of Eq. 5 into 4, yields

$$\partial_t f(\mathbf{r}, \mathbf{e}, t) + \mathbf{e} \cdot \nabla_{\mathbf{r}} f(\mathbf{r}, \mathbf{e}, t) = -\frac{f - f^{\text{eq}}}{\tau} + \frac{\mathbf{G} \cdot (\mathbf{e} - \mathbf{u})}{\rho RT} f^{\text{eq}}, \quad (6)$$

where  $\mathbf{G}$  is an external force,  $\mathbf{G} = \rho \mathbf{a}$ .

The Boltzmann equation is linked to the equations of macroscopic hydrodynamics by averaging properties over velocity space (Chapman and Cowling 1970) such that the macroscopic density,  $\rho$ , and momentum,  $\rho \mathbf{u}$  are given by

$$\rho = \int f \, d\mathbf{e}, \quad (7)$$

$$\rho \mathbf{u} = \int f \mathbf{e} \, d\mathbf{e}. \quad (8)$$

In dense fluids (e.g., liquids), the mean free path of a particle or molecule is comparable with the particle or molecular size. Thus, in addition to particle collisions, other mechanisms for momentum transfer, such as intermolecular forces must be considered. In this paper, this is simulated using the He–Shan–Doolen (HSD) model (He et al. 1998). The effective molecular interaction force  $\mathbf{F}$  can be expressed as the sum of long-range attractive and short-range repulsive forces in the form

$$\mathbf{F} = \rho \nabla V - B \rho^2 RT \chi \nabla \ln(\rho^2 \chi). \quad (9)$$

The first term in Eq. 9 arises from a mean-field approximation to the long-range intermolecular attraction and the second term is a presentation of the short-range intermolecular repulsive force.  $B$  is a function of the mass and effective diameter of a molecule and  $\chi$  is a density-dependent collision probability for molecules. The intermolecular attraction potential  $V$  has the dimensions of kinetic energy per unit mass and can be expressed as  $V = -2A\rho - \kappa \nabla^2 \rho$ .  $A$  and  $\kappa$  are parameters that are taken to be constants (He et al. 1999).

To account for the possibility that the fluid may be two-phase, with, say different densities,  $\rho_h, \rho_b$ , Eq. 9 can be recast in the form

$$\mathbf{F} = -\nabla \psi + \mathbf{F}_s, \quad (10)$$

where

$$\mathbf{F}_s = \kappa \rho \nabla \nabla^2 \rho, \quad (11)$$

represents the macroscopic interfacial force between the phases, which is associated with a steep density gradient. The parameter  $\kappa$  in Eq. 11 determines the magnitude of the interfacial tension. Bulk molecular interactions are accounted for through the potential  $\psi$  where

$$\psi = (BRT\chi - A)\rho^2, \quad (12)$$

and intermolecular potential  $\psi$  is related to the fluid pressure by  $\psi(\rho) = p - \rho RT$ . In this paper,  $\chi$  is set as

$$\chi = \frac{1 - B\rho}{(1 - B\rho/4)^3}, \quad (13)$$

then the pressure satisfies the Carnahan–Starling equation of state (Carnahan and Starling 1969) which has the form

$$p = \rho RT \frac{1 + B\rho/4 + (B\rho/4)^2 - (B\rho/4)^3}{(1 - B\rho/4)^3} - A\rho^2. \quad (14)$$

Accounting for the molecular interaction, the Boltzmann Eq. 6 for a two-phase fluid becomes

$$\begin{aligned} \partial_t f(\mathbf{r}, \mathbf{e}, t) + \mathbf{e} \cdot \nabla_{\mathbf{r}} f(\mathbf{r}, \mathbf{e}, t) = & -\frac{f - f^{\text{eq}}}{\tau} \\ & + \frac{(\mathbf{G} + \mathbf{F}_s - \nabla\psi) \cdot (\mathbf{e} - \mathbf{u})}{\rho RT} f^{\text{eq}} \end{aligned} \quad (15)$$

Specification of the intermolecular force in Eq. 15 involves the evaluation of  $\nabla\psi$ . This quantity is usually very large near interfaces and results in numerical schemes that may become unstable even for small numerical errors accumulated while calculating the intermolecular force. Hence, it is difficult to simulate multiphase flow if Eq. 15 is used directly.

To improve the stability, He et al. (1999) introduced an auxiliary distribution function, which is used to calculate pressure and velocity:

$$\xi(\mathbf{r}, \mathbf{e}, t) = f(\mathbf{r}, \mathbf{e}, t)RT + \psi(\rho)\Gamma(0), \quad (16)$$

where  $\Gamma(\mathbf{u})$  is a function of the macroscopic velocity  $\mathbf{u}$  and is given by

$$\Gamma(\mathbf{u}) = \frac{1}{(2\pi RT)^{D/2}} \exp\left[-\frac{(\mathbf{e} - \mathbf{u})^2}{2RT}\right]. \quad (17)$$

The Boltzmann equation for  $\xi$  is then obtained from Eq. 15 and is

$$\begin{aligned} \partial_t \xi + \mathbf{e} \cdot \nabla_{\mathbf{r}} \xi = & -\frac{\xi - \xi^{\text{eq}}}{\tau} + (\mathbf{e} - \mathbf{u}) \\ & \cdot [(\mathbf{F}_s + \mathbf{G})\Gamma(\mathbf{u}) + \nabla\psi(\rho)(\Gamma(0) - \Gamma(\mathbf{u}))], \end{aligned} \quad (18)$$

where

$$\xi^{\text{eq}} = RTf^{\text{eq}} + \psi(\rho)\Gamma(0). \quad (19)$$

The pressure and momentum are computed from the distribution function  $\xi(\mathbf{r}, \mathbf{e}, t)$  as follows:

$$p = \int \xi \, d\mathbf{e}, \quad (20)$$

$$\rho\mathbf{u} = \frac{1}{RT} \int \xi \, \mathbf{e} \, d\mathbf{e}. \quad (21)$$

Note that, the term involving  $\nabla\psi$  in Eq. 18 is now multiplied by a small quantity ( $\Gamma(0) - \Gamma(\mathbf{u})$ ), the numerical error in the calculation of the density gradient is greatly reduced as a result.

Rather than calculating the density distribution function, it is convenient to define an index function  $\phi$  (which represents, in some sense the phase fraction) such that

$$\phi = \int f^{\phi} \, d\mathbf{e}. \quad (22)$$

The distribution function,  $f^{\phi} = f^{\phi}(\mathbf{r}, \mathbf{e}, t)$ , for the index function  $\phi$  must be calculated as a function of time and position. This will be discussed below. The density is calculated from the index function and is

$$\rho(\phi) = \rho_l + \frac{\phi - \phi_l}{\phi_h - \phi_l} (\rho_h - \rho_l). \quad (23)$$

Here a subscript  $l$  and  $h$  on a quantity denotes the light and heavy fluid, respectively. The distribution function,  $f^{\phi}$ , for the index function  $\phi$  satisfies

$$\begin{aligned} \partial_t f^{\phi}(\mathbf{r}, \mathbf{e}, t) + \mathbf{e} \cdot \nabla_{\mathbf{r}} f^{\phi}(\mathbf{r}, \mathbf{e}, t) \\ = -\frac{f^{\phi} - f^{\phi\text{eq}}}{\tau} - \frac{\nabla\psi(\phi) \cdot (\mathbf{e} - \mathbf{u})}{RT} f^{\phi\text{eq}}, \end{aligned} \quad (24)$$

where

$$f^{\phi\text{eq}} = \frac{\phi}{(2\pi RT)^{D/2}} \exp\left[-\frac{(\mathbf{e} - \mathbf{u})^2}{2RT}\right]. \quad (25)$$

In summary, to simulate incompressible multiphase flow, two distribution functions,  $\xi$  and  $f^{\phi}$  are employed. The corresponding Boltzmann Eqs. are 18 and 24. The index distribution function  $f^{\phi}$  is used to track the density distribution through Eqs. 24, 22, and 23, while the auxiliary distribution function  $\xi$  is used to obtain the pressure and momentum fields through Eqs. 18, 20, and 21.

## 2.2 Discretization and numerical solution

The Boltzmann equations are discretized and solved numerically. Each point of the discretized physical space of interest is assigned a lattice point. Each lattice point is populated by discrete particles. These particles ‘jump’ from one lattice site to another with discrete particle velocities  $\mathbf{e}_\alpha$  ( $\alpha=0\dots b$  where  $b$  is the chosen number of discrete directions of motion), and colliding with each other at lattice nodes. Thus, the discretized form of the Boltzmann equation is referred to as the LB equation (He and Luo 1997).

To solve Eqs. 24 and 18 numerically, the following temporal discretizations are adopted:

$$\begin{aligned} f^{\phi}(\mathbf{r} + \mathbf{e} \cdot \delta t, \mathbf{e}, t + \delta t) - f^{\phi}(\mathbf{r}, \mathbf{e}, t) \\ = -\int_t^{t+\delta t} \frac{f^{\phi} - f^{\phi\text{eq}}}{\tau} dt + \int_t^{t+\delta t} \frac{\nabla\psi(\phi) \cdot (\mathbf{e} - \mathbf{u})}{RT} \Gamma(\mathbf{u}) dt, \end{aligned} \quad (26)$$

and

$$\begin{aligned} \xi(\mathbf{r} + \mathbf{e} \cdot \delta t, \mathbf{e}, t + \delta t) - \xi(\mathbf{r}, \mathbf{e}, t) = & -\int_t^{t+\delta t} \frac{\xi - \xi^{\text{eq}}}{\tau} dt \\ & + \int_t^{t+\delta t} (\mathbf{e} - \mathbf{u}) \cdot [(\mathbf{F}_s + \mathbf{G})\Gamma(\mathbf{u}) + \nabla\psi(\rho)(\Gamma(0) - \Gamma(\mathbf{u}))] dt. \end{aligned} \quad (27)$$

The integrand of the first terms on the right-hand side of Eqs. 26 and 27 is assumed to be constant over one time step. That is, the first integral in the collision operator is treated explicitly, using a first-order approximation. This assumption yields an artificial

viscosity that can be absorbed into the real viscosity of fluids (Sterling and Chen 1996). The second-order trapezoidal rule is used for the second integral (He et al. 1998). Eqs. 26 and 27 then become

$$f^\phi(\mathbf{r} + \mathbf{e} \cdot \delta t, \mathbf{e}, t + \delta t) = f^\phi(\mathbf{r}, \mathbf{e}, t) - \frac{f^\phi(\mathbf{r}, \mathbf{e}, t) - f^{\phi \text{eq}}(\mathbf{r}, \mathbf{e}, t)}{\tau / \delta t} + \left[ \frac{\nabla \psi(\phi) \cdot (\mathbf{e} - \mathbf{u})}{2RT} \Gamma(\mathbf{u}) \delta t \right]_{t+\delta t} + \left[ \frac{\nabla \psi(\phi) \cdot (\mathbf{e} - \mathbf{u})}{2RT} \Gamma(\mathbf{u}) \delta t \right]_t, \quad (28)$$

$$\begin{aligned} \tilde{\zeta}(\mathbf{r} + \mathbf{e} \cdot \delta t, \mathbf{e}, t + \delta t) &= \tilde{\zeta}(\mathbf{r}, \mathbf{e}, t) - \frac{\tilde{\zeta}(\mathbf{r}, \mathbf{e}, t) - \zeta^{\text{eq}}}{\tau / \delta t} \\ &+ \left[ (\mathbf{e} - \mathbf{u}) \cdot [(\mathbf{F}_s + \mathbf{G})\Gamma(\mathbf{u}) + \nabla \psi(\rho)(\Gamma(0) - \Gamma(\mathbf{u}))] \frac{\delta t}{2} \right]_{t+\delta t} \\ &+ \left[ (\mathbf{e} - \mathbf{u}) \cdot [(\mathbf{F}_s + \mathbf{G})\Gamma(\mathbf{u}) + \nabla \psi(\rho)(\Gamma(0) - \Gamma(\mathbf{u}))] \frac{\delta t}{2} \right]_t. \end{aligned} \quad (29)$$

The following variable transformations are introduced:

$$\tilde{f} = f^\phi + \frac{(\mathbf{e} - \mathbf{u}) \cdot \nabla \psi(\phi)}{2RT} \Gamma(\mathbf{u}) \delta t, \quad (30)$$

$$\begin{aligned} \tilde{\zeta} &= \zeta - \frac{1}{2}(\mathbf{e} - \mathbf{u}) \\ &\cdot [(\mathbf{F}_s + \mathbf{G})\Gamma(\mathbf{u}) + \nabla \psi(\rho)(\Gamma(0) - \Gamma(\mathbf{u}))] \delta t. \end{aligned} \quad (31)$$

Then Eqs. 28 and 29 transform to

$$\begin{aligned} \tilde{f}(\mathbf{r} + \mathbf{e} \cdot \delta t, \mathbf{e}, t + \delta t) &= \tilde{f}(\mathbf{r}, \mathbf{e}, t) - \frac{\tilde{f}(\mathbf{r}, \mathbf{e}, t) - f^{\text{eq}}(\mathbf{r}, \mathbf{e}, t)}{\tau / \delta t} \\ &+ \frac{(2\tau - \delta t) \nabla \psi(\phi) \cdot (\mathbf{e} - \mathbf{u})}{2\tau RT} \Gamma(\mathbf{u}) \delta t, \end{aligned} \quad (32)$$

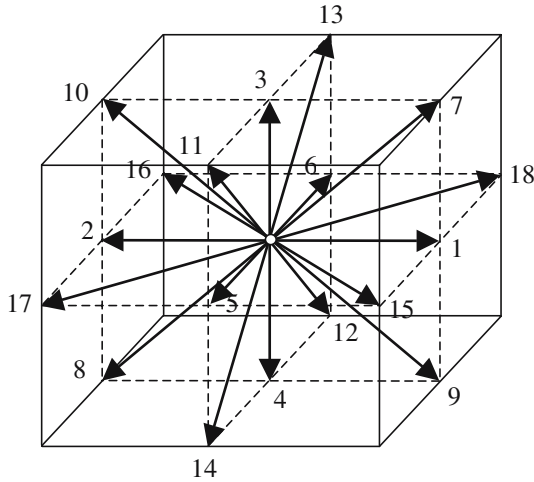


**Fig. 1** Three-dimensional lattice (D3Q19) geometry and discretized velocity vector space

and

$$\begin{aligned} \tilde{\zeta}(\mathbf{r} + \mathbf{e} \cdot \delta t, \mathbf{e}, t + \delta t) &= \tilde{\zeta}(\mathbf{r}, \mathbf{e}, t) - \frac{\tilde{\zeta}(\mathbf{r}, \mathbf{e}, t) - \zeta^{\text{eq}}(\mathbf{r}, \mathbf{e}, t)}{\tau / \delta t} + \frac{2\tau - \delta t}{2\tau} \\ &\cdot \left[ (\mathbf{e} - \mathbf{u}) \cdot [(\mathbf{F}_s + \mathbf{G})\Gamma(\mathbf{u}) + \nabla \psi(\rho)(\Gamma(0) - \Gamma(\mathbf{u}))] \frac{\delta t}{2} \right]. \end{aligned} \quad (33)$$

To obtain the LB model, the velocity space must be discretized as mentioned earlier. A so-called D3Q19 discretization (Mei et al. 2000) is employed in this paper (see Fig. 1). There are 19 discrete lattice velocities that are defined as:

$$\mathbf{e}_\alpha = \begin{cases} (0, 0, 0) & \alpha = 0 \\ (\pm c, 0, 0), (0, \pm c, 0), (0, 0, \pm c) & \alpha = 1 \sim 6 \\ (\pm c, \pm c, 0), (\pm c, 0, \pm c), (0, \pm c, \pm c) & \alpha = 7 \sim 18 \end{cases}. \quad (34)$$

Note that the calculated distribution functions at the next time step using this discretization may not reside on the grid nodes. A reconstruction step is necessary to extrapolate the information onto the grid nodes. There are many options for this reconstruction step. For isothermal flow, the computation can be greatly simplified if the physical space can be discretized so that every discrete distribution function travels from one grid node to another grid node in each time step. That is, every  $\mathbf{r} + \mathbf{e}_\alpha \delta t$  lies exactly on a grid node. This is done simply by setting  $c = \delta x / \delta t = 1$ , that is, the regular lattice has a lattice length of  $c\delta t$ . This also leads to the definition of the so-called ‘LBE sound speed’ (He and Luo 1997) as:

$$c^2 = 3c_s^2 = 3RT, \quad (35)$$

where  $c_s = \sqrt{RT}$ .

Each lattice velocity is assigned a pair of discrete distribution functions,  $\tilde{f}_\alpha, \tilde{\zeta}_\alpha, \alpha = 0 \dots 18$ , that are defined by

$$\tilde{f}_\alpha(\mathbf{r}, t) = w_\alpha \tilde{f}(\mathbf{r}, \mathbf{e}_\alpha, t), \quad (36)$$

$$\tilde{\zeta}_\alpha(\mathbf{r}, t) = w_\alpha \tilde{\zeta}(\mathbf{r}, \mathbf{e}_\alpha, t), \quad (37)$$

where the  $w_\alpha$  are ‘weights’ with the following values for a D3Q19 lattice model (Mei et al. 2000):

$$w_\alpha = \begin{cases} 1/3 & \alpha = 0 \\ 1/18 & \alpha = 1 \sim 6 \\ 1/36 & \alpha = 7 \sim 18 \end{cases}. \quad (38)$$

The function  $\Gamma(\mathbf{u})$  can be expanded in terms of Mach number  $(\mathbf{u}/c_s)$  in a Taylor series and has the form

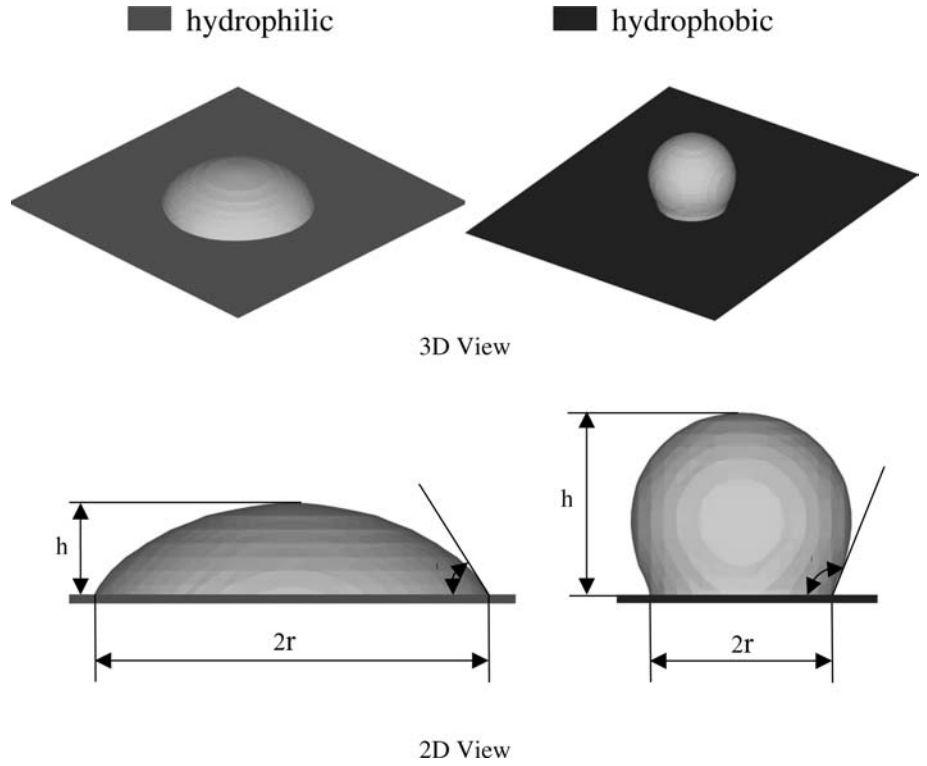
$$\Gamma_\alpha(\mathbf{u}) = w_\alpha \left[ 1 + \frac{(\mathbf{e}_\alpha \cdot \mathbf{u})}{c_s^2} + \frac{(\mathbf{e}_\alpha \cdot \mathbf{u})^2}{2c_s^4} - \frac{\mathbf{u}^2}{2c_s^2} \right] + O(\mathbf{u}^3/c_s^3). \quad (39)$$

The equilibrium distribution functions of  $f_\alpha$  and  $\zeta_\alpha$  are

$$f_\alpha^{\text{eq}}(\mathbf{u}) = \phi \Gamma_\alpha(\mathbf{u}), \quad (40)$$



**Fig. 2** Droplet spreading on a homogenous surface



and

$$\xi_\alpha^{\text{eq}}(\mathbf{u}) = w_\alpha p + \rho c_s^2 (\Gamma_\alpha(\mathbf{u}) - 1). \quad (41)$$

With the velocity space discretization described above applied to Eqs. 32 and 33, the discrete distribution functions  $\tilde{f}_\alpha$  and  $\tilde{\xi}_\alpha$  satisfy the following evolution equations:

$$\begin{aligned} \tilde{f}_\alpha(\mathbf{r} + \mathbf{e}_\alpha \delta t, t + \delta t) = & \tilde{f}_\alpha(\mathbf{r}, t) - \frac{\tilde{f}_\alpha(\mathbf{r}, t) - f_\alpha^{\text{eq}}(\mathbf{r}, t)}{\tau / \delta t} \\ & + \frac{(2\tau - \delta t) \nabla \psi(\phi) \cdot (\mathbf{e}_\alpha - \mathbf{u})}{2\tau RT} \Gamma_\alpha(\mathbf{u}) \delta t, \end{aligned} \quad (42)$$

$$\begin{aligned} \tilde{\xi}(\mathbf{r} + \mathbf{e}_\alpha \delta t, t + \delta t) = & \tilde{\xi}_\alpha(\mathbf{r}, t) - \frac{\tilde{\xi}_\alpha(\mathbf{r}, t) - \xi_\alpha^{\text{eq}}(\mathbf{r}, t)}{\tau / \delta t} + \frac{2\tau - \delta t}{2\tau} \\ & \cdot \left[ (\mathbf{e}_\alpha - \mathbf{u}) \cdot [(\mathbf{F}_s + \mathbf{G}) \Gamma_\alpha(\mathbf{u}) + \nabla \psi(\rho) (\Gamma_\alpha(0) - \Gamma_\alpha(\mathbf{u}))] \frac{\delta t}{2} \right]. \end{aligned} \quad (43)$$

The macroscopic variables can now be calculated using

$$\phi = \sum_{\alpha=0}^{18} \tilde{f}_\alpha, \quad (44)$$

$$p = \sum_{\alpha=0}^{18} \tilde{\xi}_\alpha - \frac{1}{2} \mathbf{u} \cdot \nabla \psi(\rho) \delta t, \quad (45)$$

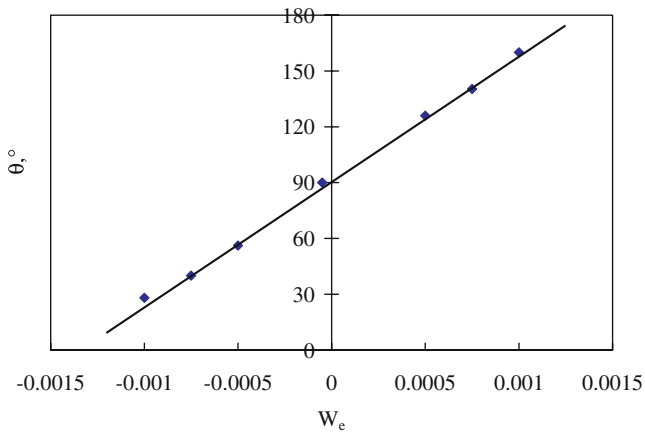


**Fig. 3** Contact angle vs. interaction strength parameter  $W_e$

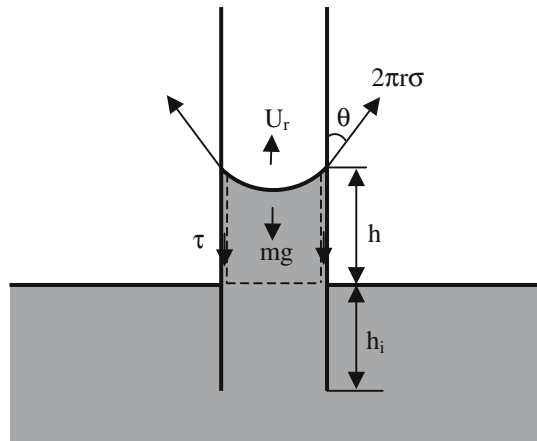


**Fig. 4** Forces acting on a liquid column during capillary rise

**Table 1** Parameters for simulation of capillary rise

Unit	$\rho_1$	$\rho_2$	$\nu$	$\sigma$	$\theta$	$H_i$
Lattice	0.1	1.5	0.04	0.022	75	45
Metric	62 kg/m <sup>3</sup>	937 kg/m <sup>3</sup>	8.0×10 <sup>-6</sup> m <sup>2</sup> /s	0.027 N/m	75°	900 μm

$$\rho \mathbf{u} = \frac{1}{RT} \sum_{\alpha=0}^{18} \mathbf{e}_\alpha \tilde{\xi}_\alpha + \frac{\delta t}{2} (\mathbf{F}_s + \mathbf{G}). \quad (46)$$

The relaxation time,  $\tau$  is a parameter which characterizes the constitutive behavior of the fluent material at a microscopic level. It is connected with the macroscopic kinematic viscosity of the simulated fluid according to

$$\nu = (\tau - 0.5 \delta t) c_s^2. \quad (47)$$

To model phases with different viscosity, the relaxation time  $\tau$  should be a variable which depends on index function  $\phi$ . For example,

$$\tau(\phi) = A\phi + B, \quad (48)$$

with

$$\begin{aligned} \tau(\phi_h) &= \tau_h, \\ \tau(\phi_l) &= \tau_l. \end{aligned} \quad (49)$$

Combining Eqs. 48 and 49 gives

$$\tau(\phi) = \tau_l + \frac{\phi - \phi_l}{\phi_h - \phi_l} (\tau_h - \tau_l), \quad (50)$$

which corresponds the variable kinematic viscosity

$$\nu(\phi) = \left( \tau_l + \frac{\phi - \phi_l}{\phi_h - \phi_l} (\tau_h - \tau_l) \right) c_s^2. \quad (51)$$

The discretization scheme used here leads to an apparent kinematic viscosity given by

$$\nu_{app}(\phi) = \left( \tau_l + \frac{\phi - \phi_l}{\phi_h - \phi_l} (\tau_h - \tau_l) - \frac{1}{2} \delta t \right) c_s^2, \quad (52)$$

and the viscosities of the pure phases,  $h$  and  $l$  are  $\nu_h = (\tau_h - 0.5 \delta t) c_s^2$  and  $\nu_l = (\tau_l - 0.5 \delta t) c_s^2$ , respectively.

### 2.3 Wetting solid surface boundary conditions

In the simulations the no-slip boundary condition at solid–fluid interfaces is realized through a computationally efficient ‘bounce-back’ condition (Succi 2001), where the particle momenta are conserved during collisions with a solid wall. Adhesive forces between the fluid and solid wall are introduced into the model by Martys (1996) and can be expressed as

$$\mathbf{F}_{ad}(\mathbf{r}) = -\tau E(\mathbf{r}) \sum_{\alpha=0}^{18} W_\alpha s(\mathbf{r} + \mathbf{e}_\alpha) \mathbf{e}_\alpha, \quad (53)$$

where

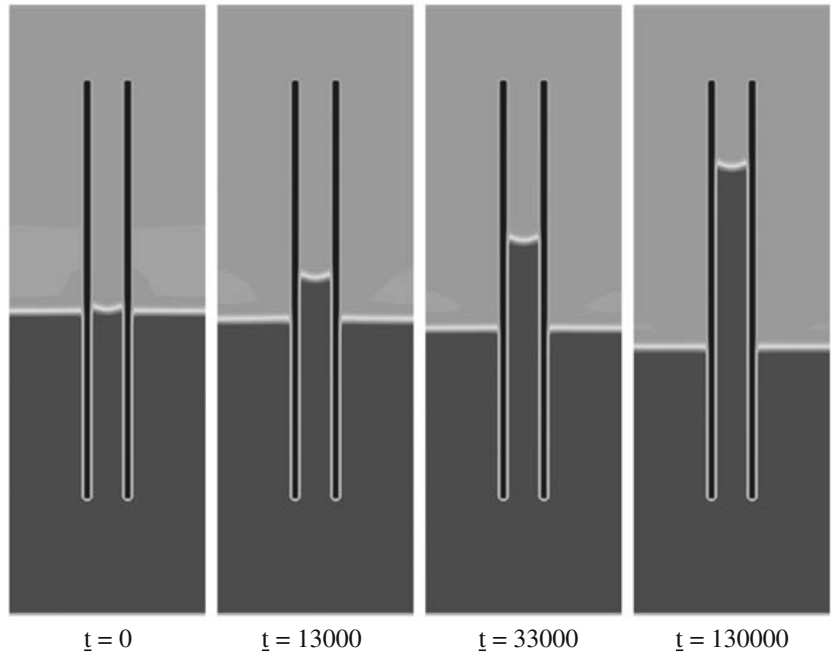
$$E(\mathbf{r}) = \rho_0 \{1 - \exp[-\rho(\mathbf{r})/\rho_0]\}. \quad (54)$$

where  $\rho_0 = (\rho_h + \rho_l)/2$  and

$$W_\alpha = \begin{cases} 4W_e & \text{for } |e_\alpha| = 1 \\ W_e & \text{for } |e_\alpha| = \sqrt{2}. \\ 0 & \text{for } |e_\alpha| = 0 \end{cases}. \quad (55)$$

Here  $s=0,1$  for nodes in the liquid and nodes on solid walls, respectively.  $W_e$  represents the particle interaction

**Fig. 5** Capillary rise in a tube with radius  $r = 140 \mu\text{m}$  in weightlessness ( $Bo = 0$ )



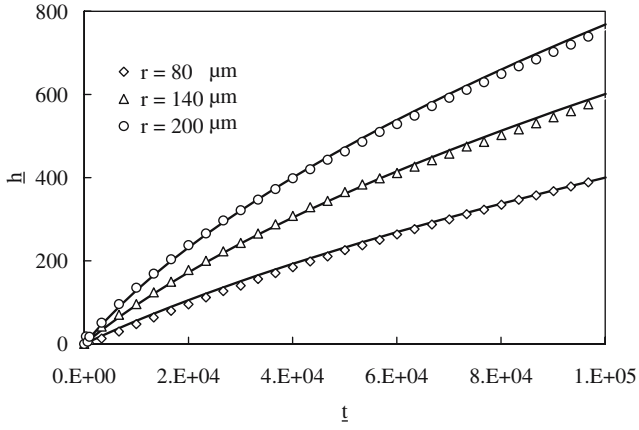


**Fig. 6** Capillary rise height vs. time for different tube radii ( $Bo=0$ )

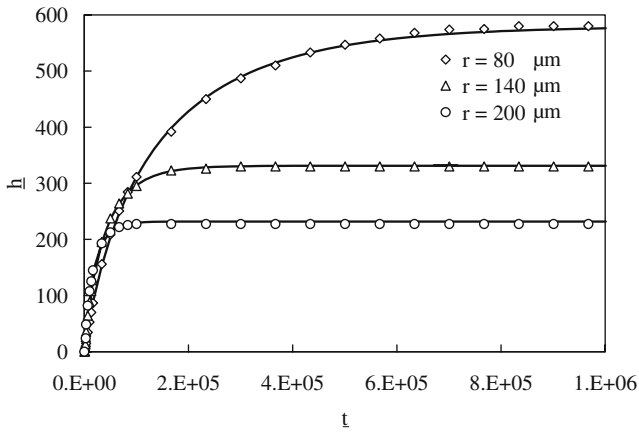


**Fig. 7** Capillary rise height vs. time for different tube radii ( $Bo=2.7 \times 10^{-5}$ )

strength between fluid and solid walls, and is positive for a hydrophobic surface and negative for a hydrophilic surface. With these definitions the interfacial tension force, adhesive force and body force change the momenta of fluid particles at each time step and Eq. 46 becomes

$$\rho \mathbf{u} = \frac{1}{c_s^2} \sum_{\alpha=0}^{18} \mathbf{e}_\alpha \tilde{\zeta}_\alpha + \frac{\delta t}{2} (\mathbf{F}_s + \mathbf{F}_{ad} + \rho \mathbf{g}). \quad (56)$$

#### 2.4 Outline of solution procedure

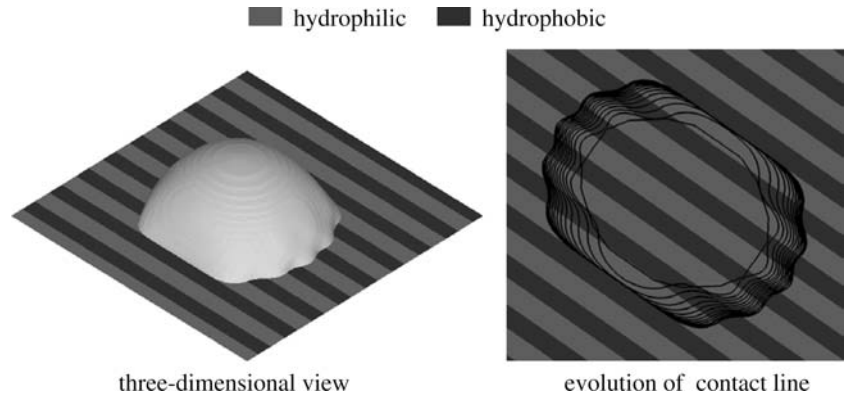
Combining Eqs. 42, 43, and 53, the velocity, pressure and density distributions are solved at each time step as follows:

- Set an initial velocity  $\mathbf{u}$ , density  $\rho$ , index function  $\phi$ , pressure  $p$  at each site in the domain field.
- Calculate equilibrium distribution functions  $f_\alpha^{eq}(\mathbf{r}, t)$  and  $\zeta_\alpha^{eq}(\mathbf{r}, t)$  with Eqs. 40 and 41 at each site.
- Calculate the surface tension force  $\mathbf{F}_s$  and adhesive force  $\mathbf{F}_{ad}$  using Eqs. 11 and 53, respectively.
- Complete the collision and propagation using Eqs. 42 and 43 to obtain distribution functions  $f_\alpha(\mathbf{r}, t)$  and  $\zeta_\alpha(\mathbf{r}, t)$  at the new time step.
- Calculate  $\phi$ ,  $\rho$ ,  $p$  and  $\mathbf{u}$  with Eqs. 44, 23, 45 and 56 for the new time step.
- Return to step (b) and repeat until either a steady state/equilibrium is obtained or, for time-dependent flows, until the desired time has elapsed.

Before carrying out any dynamic simulations, we first need to obtain relationships between the simulation parameters  $\kappa$ ,  $\tau$  and  $W_e$  and macroscopic quantities corresponding to surface tension, viscosity and equilibrium contact angle. While the viscosity can be calculated directly by Eq. 47, the surface tension and equilibrium contact angle  $\theta$  require to be determined by carrying out a series of simulations that mimic experimental measurements of these quantities. For example, the relationship between  $W_e$  and  $\theta$  is found by picking a fixed value of  $W_e$ , simulating a static drop on a horizontal solid surface and measuring the drop height  $h$  and the radius  $r$  of the circular contact region between the droplet and surface (see Fig. 2). The contact angle is measured by

$$\theta = \arcsin\left(\frac{2rh}{r^2 + h^2}\right). \quad (57)$$

**Fig. 8** Long time configurations of a spreading droplet on a heterogeneous surface.  $\delta_{phi} = 140 \mu\text{m}$ ,  $\delta_{pho} = 100 \mu\text{m}$ ,  $\theta_{phi} = 40^\circ$ ,  $\theta_{pho} = 110^\circ$ ,  $g = 9.8 \text{ m/s}^2$





Note that, consistent with the definition of an equilibrium contact angle, Eq. 57 is valid for a drop with a semicircular contact line.

The relation between contact angle and the parameter  $W_e$  is determined by using a computational domain with  $100 \times 100 \times 50$  grid nodes. To relate the simulation parameters to real physical quantities, a length scale  $L_0$ , time scale  $t_0$  and mass scale  $M_0$  are required to be determined. A simulation parameter with dimension  $[L]^{n_1} [t]^{n_2} [M]^{n_3}$  is multiplied by  $[L_0]^{n_1} [t_0]^{n_2} [M_0]^{n_3}$  to give the physical quantities. In this simulation,  $L_0 = 2.0 \times 10^{-5}$  m,  $t_0 = 2.0 \times 10^{-6}$  s,  $M_0 = 5.0 \times 10^{-12}$  kg were chosen to give real physical length, density, viscosity and surface tension.

The fluid region is initially composed of a hemispherical liquid droplet in contact with hydrophilic or hydrophobic substrate and the vapor phase elsewhere. The system is then allowed to evolve and the drop either spreads to increase the solid/liquid contact area or contract to decrease the contact area, depending on the

property of the substrate. Figure 2 shows the evolved equilibrium droplet with a static contact angle. The density of the droplet and surrounding fluid is 937 and 62 kg/m<sup>3</sup>, respectively. The parameter  $\kappa$  is set to be  $\kappa = 0.04$  that corresponds to a surface tension of  $\sigma_s = 0.027$  N/m. The results are shown in Fig. 3 and fit the linear equation given below

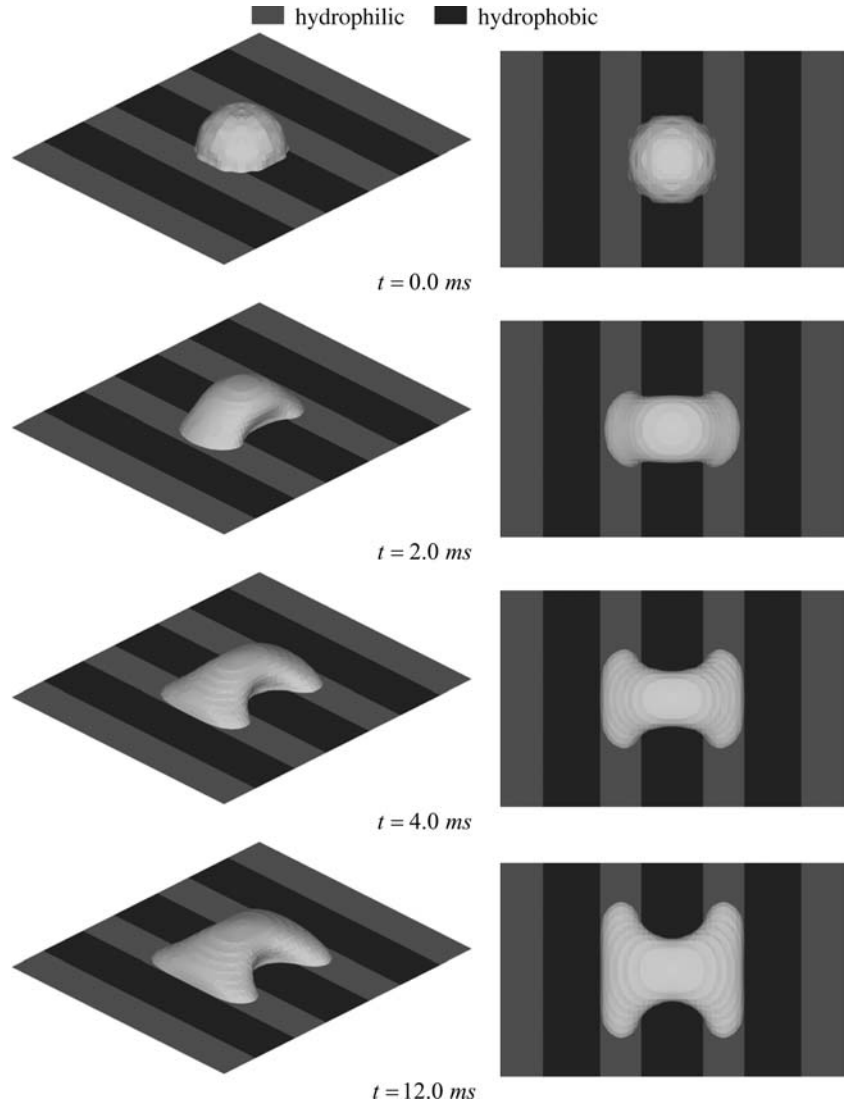
$$\theta = 67710 \times (W_e + 0.0013291) \text{ deg.} \quad (58)$$

### 3 Results and discussion

#### 3.1 Verification of ‘measured’ wetting properties

A reliable correlation between  $\theta$  and  $W_e$  is needed if the LB model is to be used with confidence as a predictive model. To test the ‘measured’ values a numerical experiment with capillary rise was undertaken that provides a useful benchmark. Figure 4 shows the geometry of the capillary rise process considered. For a

**Fig. 9** Droplet spreading on a heterogeneous surface. The initial droplet is located on the centerline of the hydrophobic strip.  $\delta_{\text{phi}} = 160 \mu\text{m}$ ,  $\delta_{\text{pho}} = 260 \mu\text{m}$ ,  $\theta_{\text{phi}} = 40^\circ$ ,  $\theta_{\text{pho}} = 110^\circ$ ,  $g = 9.8 \text{ m/s}^2$



tube with a radius  $r$  inserted into a fluid, the fluid column should rise if the fluid is wetting (contact angle  $\theta < 90^\circ$ ) or fall with non-wetting fluid (contact angle  $\theta > 90^\circ$ ). It is possible from a simple theory to predict the velocity at which the fluid column rises as well as the time it takes. For the simulations presented here we assume that the contact angle  $\theta$  is independent of velocity, the resistance to flow comes only from the fluid viscosity, which is the same in both phases (i.e.,  $v_h = v_l = v$ ). The fluid in the tube rises as a function of time and can be easily determined by

$$(h + h_i) \frac{dh}{dt} + \frac{r^2 g}{8v} h - \frac{r\sigma \cos \theta}{4v\rho_2} = 0 \quad (59)$$

where  $h$  is the instantaneous position of the meniscus of the fluid column in the tube,  $h_i$  is the length of the part of the capillary tube immersed in the liquid, and  $r$  is the radius of the tube with a circular cross section. Fluid density, viscosity, surface tension and contact angle are denoted by  $\rho_2$ ,  $v$ ,  $\sigma$  and  $\theta$ , respectively.

The Eq. 59 can be non-dimensionalized by using the characteristic time  $t_{\text{ref}} = \rho_2^2 v^3 / \sigma^2$  and length  $l_{\text{ref}} = \rho_2 v^2 / \sigma$  to yield

$$(\underline{h} + \underline{h}_i) \frac{d\underline{h}}{d\underline{t}} + \frac{1}{8} \underline{r}^2 \underline{Bo} \underline{h} - \frac{1}{4} \underline{r} \cos \theta = 0 \quad (60)$$

where  $Bo$  is the Bond number  $Bo = g\rho_2^3 v^4 / \sigma^3$ , and an under bar denotes a dimensionless variable.

If there is no gravity, i.e.,  $Bo = 0$ , Eq. 60 simplifies to

$$\underline{h} = -\underline{h}_i + \sqrt{\underline{h}_i^2 + \frac{1}{2} \underline{r} \cos \theta \underline{t}}. \quad (61)$$

The verification simulation of capillary rise with multiphase LBM was carried out on a three-dimensional domain with a  $70 \times 70 \times 200$  lattice nodes for tube radii  $r = 4, 7, \text{ and } 10$  lattices which correspond metric units  $r = 80, 140, \text{ and } 200 \mu\text{m}$  and dimensionless radii  $\underline{r} = 36.5, 64.0, \text{ and } 91.3$ , respectively. The parameters for each simulation are listed in Table 1.

**Fig. 10** Droplet spreading on a heterogeneous surface. The initial displacement of the center of the droplet from the centerline of the hydrophobic strip is  $40 \mu\text{m}$ .  $\delta_{\text{phi}} = 160 \mu\text{m}$ ,  $\delta_{\text{pho}} = 260 \mu\text{m}$ ,  $\theta_{\text{phi}} = 40^\circ$ ,  $\theta_{\text{pho}} = 110^\circ$ ,  $g = 9.8 \text{ m/s}^2$

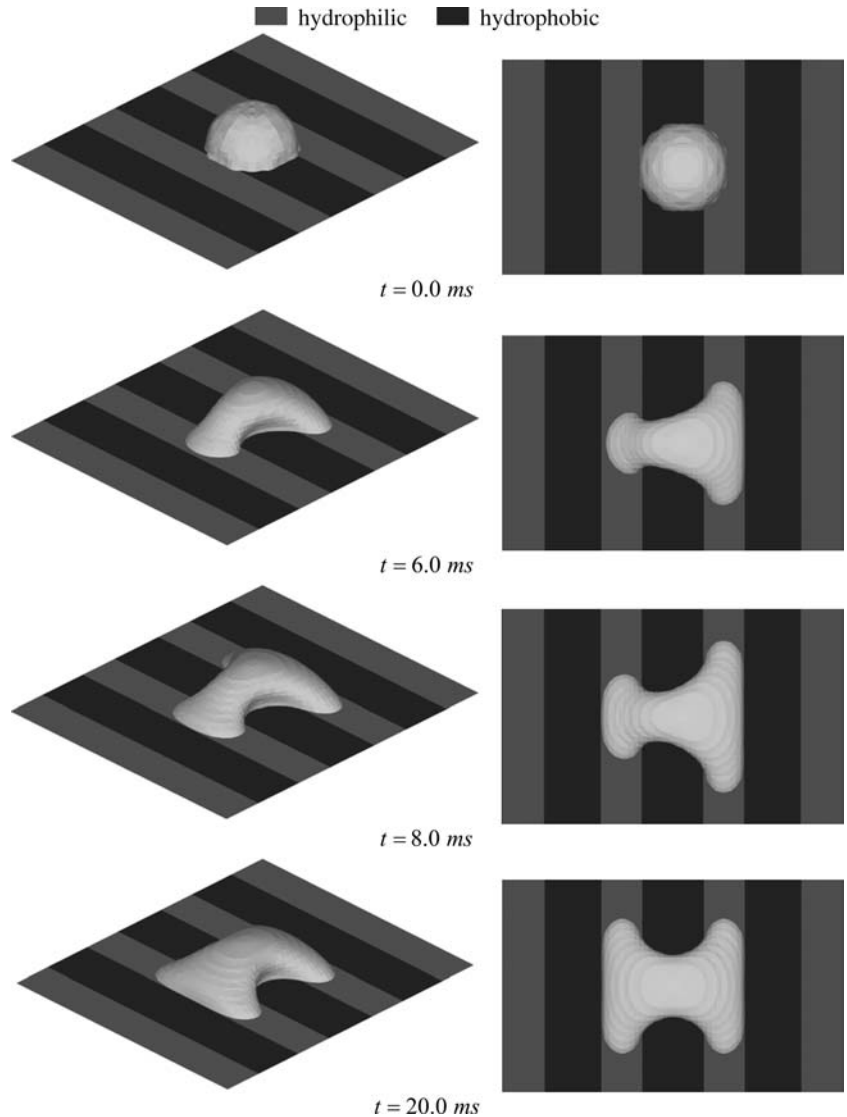


**Fig. 11** Droplet spreading on a heterogeneous surface. The initial displacement of the center of the droplet from the centerline of the hydrophobic strip is  $80\ \mu\text{m}$ .  $\delta_{\text{phi}} = 160\ \mu\text{m}$ ,  $\delta_{\text{pho}} = 260\ \mu\text{m}$ ,  $\theta_{\text{phi}} = 40^\circ$ ,  $\theta_{\text{pho}} = 110^\circ$ ,  $g = 9.8\ \text{m/s}^2$

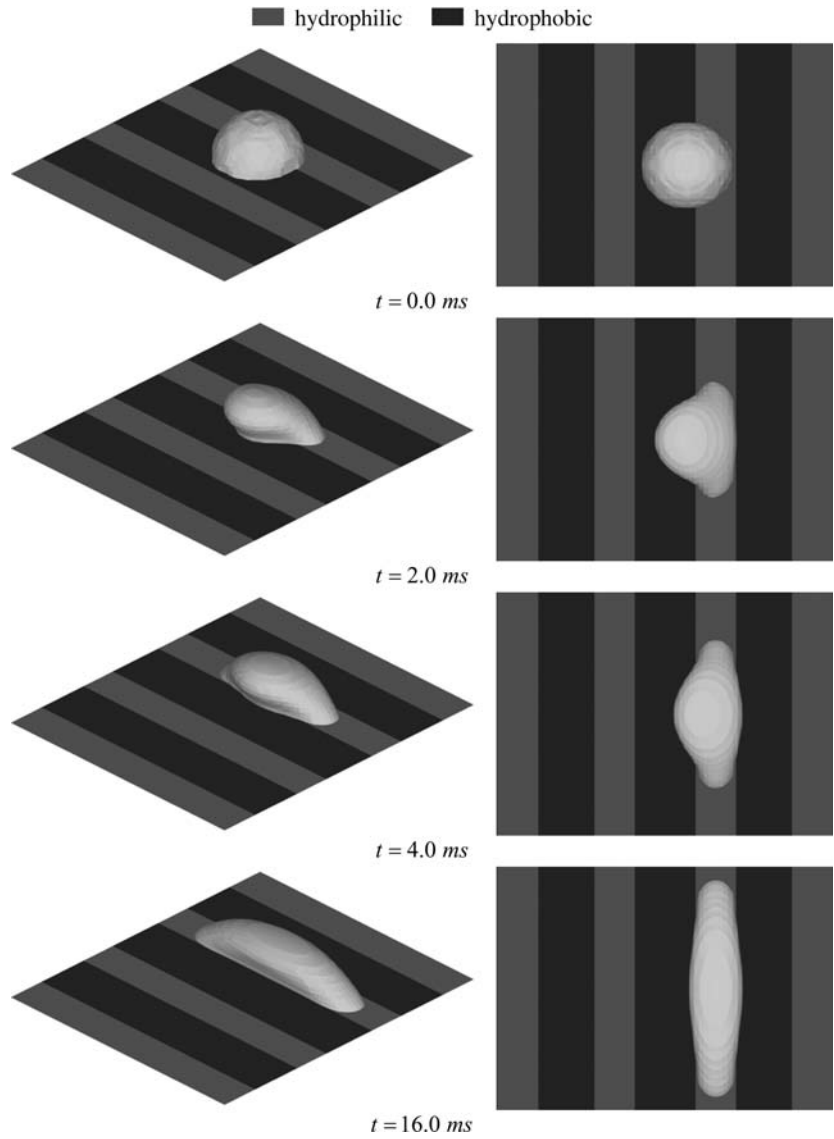


**Fig. 12** Equilibrium shape of droplet after spreading on a heterogeneous surface. The initial droplet is located on the centerline of the hydrophobic strip.  $\delta_{\text{phi}} = 300\ \mu\text{m}$ ,  $\delta_{\text{pho}} = 260\ \mu\text{m}$ ,  $\theta_{\text{phi}} = 40^\circ$ ,  $\theta_{\text{pho}} = 110^\circ$ ,  $g = 9.8\ \text{m/s}^2$

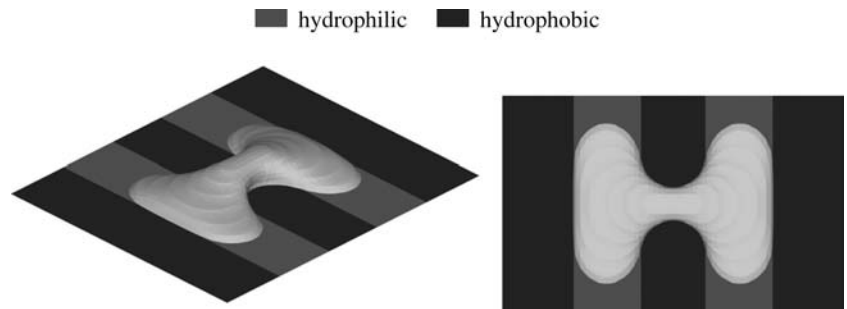
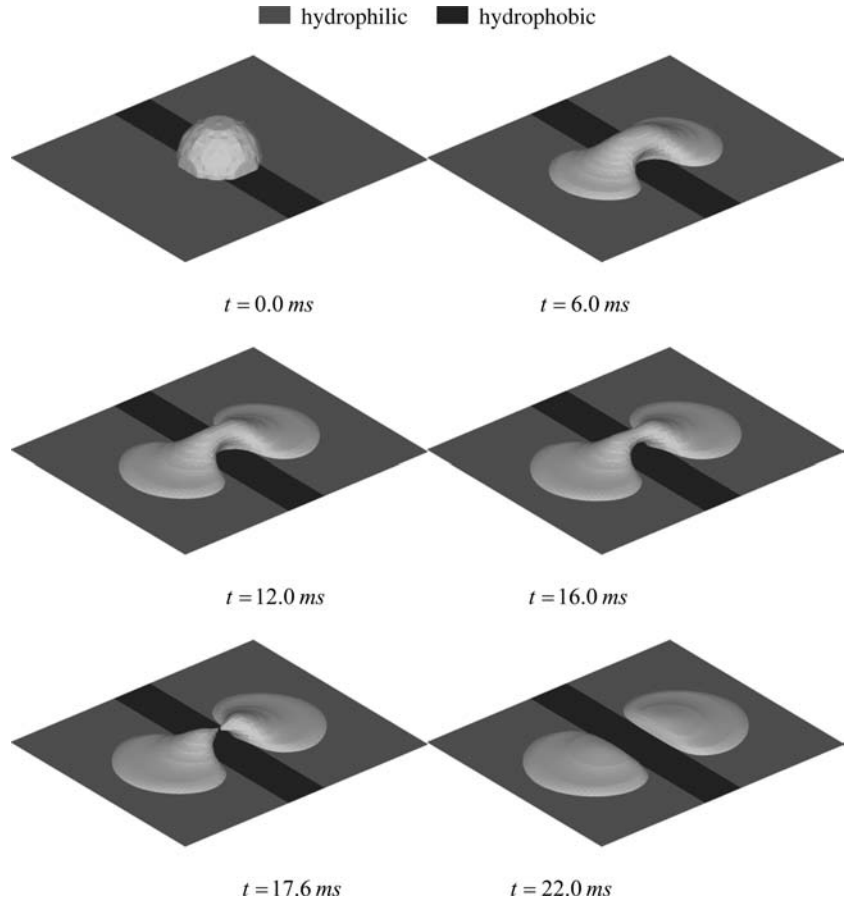


Figure 5 presents the dynamic motion of the fluid in the capillary tube for  $r = 140\ \mu\text{m}$  under weightlessness ( $Bo = 0$ ). The horizontal boundary conditions are periodic while the top/bottom and tube wall are assumed to be ‘bounce-back’ boundaries (Succi 2001). The contact angle of the fluid against the outside wall of the tube is set to be  $\pi/2$ . Figure 6 presents the

instantaneous height of the capillary rise under weightlessness. The solid lines in the figure show the corresponding theoretical solution of Eq. 61. The figure also reveals that there is no limit to the capillary rise height in weightlessness.

Comparisons between multiphase LBM simulation results and theoretical solution at  $g = 9.8\ \text{m/s}^2$  ( $Bo = 2.7$

**Fig. 13** Snapshots of droplet spreading and its breakup on a heterogeneous surface. The initial droplet is located on the centerline of the hydrophobic strip.  $\delta_{\text{phi}} = \infty$ ,  $\delta_{\text{pho}} = 200 \mu\text{m}$ ,  $\theta_{\text{phi}} = 20^\circ$ ,  $\theta_{\text{pho}} = 160^\circ$ ,  $g = 9.8 \text{ m/s}^2$



$\times 10^{-5}$ ) are shown in Fig. 7. As expected, the gravity retards the rise and an equilibrium height is approached. The simulation results shown in Figs. 6 and 7 agree well with the theoretical solution for both weightless and non-zero gravity conditions.

### 3.2 Single droplet spanning several hydrophilic-hydrophobic stripes

A simple heterogeneous surface consisting of alternating and parallel strips with different surface wetting properties was considered. The hydrophilic and hydrophobic strips are characterized by widths  $\delta_{\text{phi}}$ ,  $\delta_{\text{pho}}$ , respectively. A single component liquid drop that forms an intrinsic contact angle  $\theta_{\text{phi}}$ ,  $\theta_{\text{pho}}$  separately on each surface and  $0 \leq \theta_{\text{phi}} \leq \theta_{\text{pho}} \leq \pi$ . The strip width and contact angle have values of  $\delta_{\text{phi}} = 140 \mu\text{m}$ ,  $\delta_{\text{pho}} = 100 \mu\text{m}$ , and  $\theta_{\text{phi}} = 40^\circ$ ,  $\theta_{\text{pho}} = 110^\circ$ , respectively. Unless otherwise mentioned, the density and viscosity of the droplet and surrounding fluid are set to be  $\rho_h = 937 \text{ kg/m}^3$ ,  $\rho_l = 62 \text{ kg/m}^3$ ,  $\nu_h = 8.0 \times 10^{-6} \text{ m}^2/\text{s}$ ,  $\nu_l = 1.0 \times 10^{-6} \text{ m}^2/\text{s}$ , respectively, and surface tension  $\sigma = 0.027 \text{ N/m}$ .

The behavior of a hemispherical droplet with a radius  $r = 400 \mu\text{m}$  spreading on such a surface is shown in Fig. 8. At beginning, the droplet rapid spreads out in all directions. When the contact line parallel to the strips

approaches the edge of a hydrophobic strip, the spreading rate in this direction slows, ultimately stops, and is pinned at the edge. The droplet then spreads along the strips until an equilibrium state is reached. Despite the fact that the droplet is initially situated at a location other than the centerline of the middle strip, the final state is symmetric. The equilibrium contact line shown in Fig. 8b shows the pattern of the underlying substrate and agrees qualitatively with experimental results obtained by Pompe et al. (1998).

### 3.3 Droplet spanning three strips

Figure 9 shows the evolution of a small hemispherical droplet spreading on heterogeneous surface with relative wider strips. The initial droplet has a radius  $r = 200 \mu\text{m}$  and is located on the centerline of the hydrophobic strip. The strip width and contact angle have the value  $\delta_{\text{phi}} = 160 \mu\text{m}$ ,  $\delta_{\text{pho}} = 260 \mu\text{m}$ , and  $\theta_{\text{phi}} = 40^\circ$ ,  $\theta_{\text{pho}} = 110^\circ$ , respectively. As shown in Fig. 9, the droplet stretches over both hydrophilic strips due to the attractive force of the hydrophilic surfaces. At the same time, the drop rapidly contracts inward along the hydrophobic strip and the central height of the droplet decreases at the initial stage and slightly increases after time  $t = 4.0 \text{ ms}$ . Viewed from top, the drop has an 'H' shape, with the connecting bar located over the hydrophobic

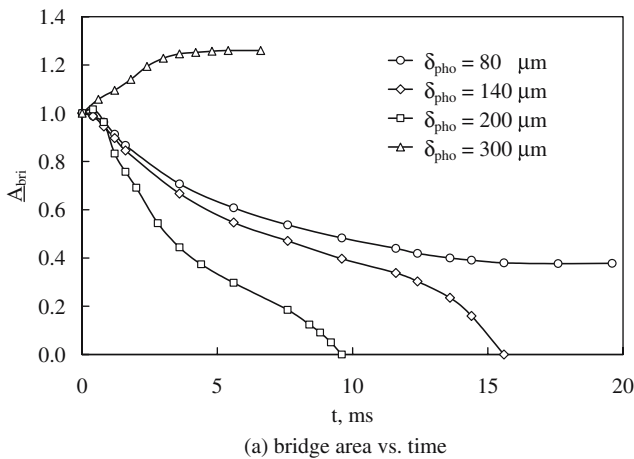
strip. Note that the droplet remains symmetric both about an axis parallel to the stripes and about an axis perpendicular to the stripes in the whole spreading process. Finally, the droplet approaches an equilibrium state and spreading ceases at time  $t = 12.0$  ms. A dimensionless time  $\underline{t} = \sigma t / (\rho_2 v_2 r)$  is introduced in order to compare with the experimental results. The dimensionless time is  $\underline{t} = 0.15$  (corresponding a spreading time  $t = 12.0$  ms) which is too short compared with the experimental result (Zosel 1993). This is due to the width of the interface being too large and the density difference being too small (Dupuis and Yeomans 2004).

### 3.4 Effect of the initial location of droplet on spreading process

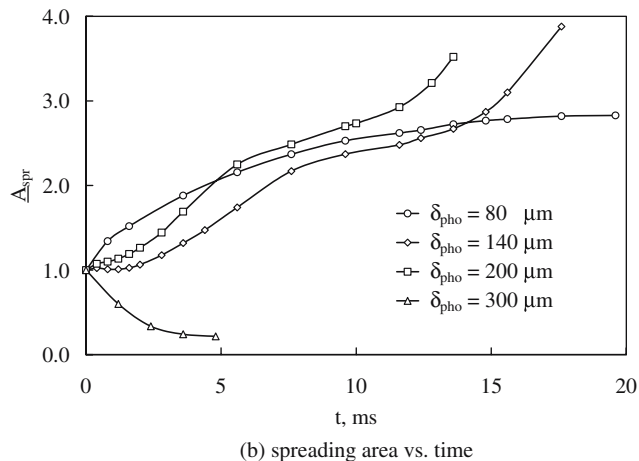
One important factor that affects the spreading dynamics of droplet on a heterogeneous surface is the initial position of the droplet. Different with Fig. 9, in this case the droplet is initially placed such that its center is located  $40 \mu\text{m}$  off the centerline of the middle

hydrophobic strip. The results are shown in Fig. 10. Because the initial droplet is closer to the right hydrophilic strip, it spreads towards the right faster in the early stage of spreading. The droplet remains symmetric about an axis perpendicular to the stripes while it becomes asymmetric about the centerline of the middle hydrophobic strip. However, the left hydrophilic strip drags the droplet more toward the left hydrophilic strip in the later stages of spreading. The final equilibrium state is identical to that shown in Fig. 9d, where the final drop was symmetric about the centerline of the middle hydrophobic strip. However, the approach to equilibrium for off-centered drop takes longer.

For a larger initial displacement of the center of the droplet from the centerline of the hydrophobic strip, for instance,  $80 \mu\text{m}$ , the drop only moves toward the nearest hydrophilic strip. As shown in Fig. 11, the droplet slips toward the right hydrophilic strip and then stretches on it. Compared with the results simulated by Leopoldes et al. (2003) and Dupuis and Yeomans (2004), which are based on free-energy model, the droplet behaviors in Figs. 9, 10, and 11 show a similar tendency.

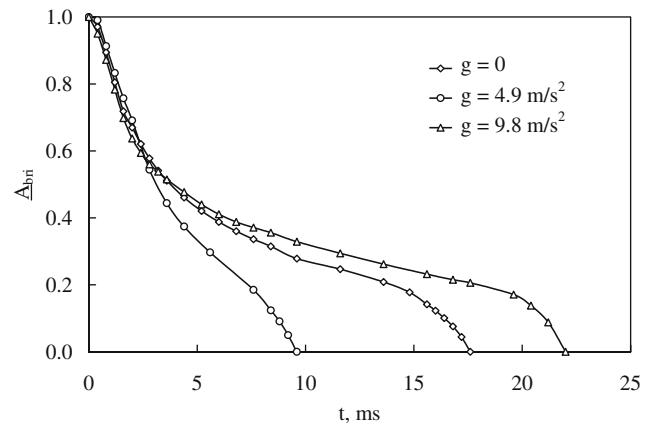


(a) bridge area vs. time

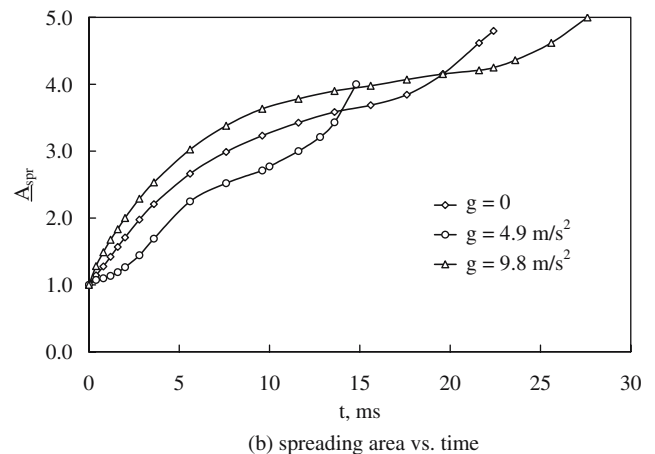


(b) spreading area vs. time

**Fig. 14** Effect of the hydrophobic strip width on spreading dynamics



(a) bridge area vs. time



(b) spreading area vs. time

**Fig. 15** Effect of gravity on spreading dynamics



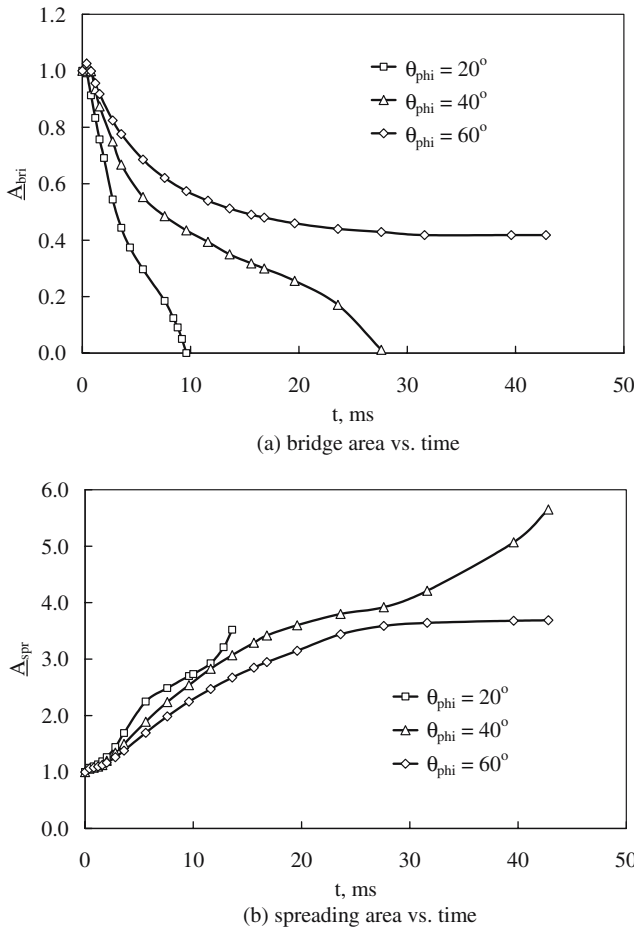


**Fig. 16** Effect of the contact angle on the hydrophilic surface on spreading dynamics

### 3.5 Droplet spreading and breakup

If the width of the hydrophilic strip is increased and all other conditions are kept the same as for the case shown in Fig. 9, the droplet can spread further on the hydrophilic strip. The wider hydrophilic strip thins the portion of the droplet on the hydrophobic strip and a neck forms (see Fig. 12). This example motivated us to investigate the conditions that lead to breakup of the drop.

For a uniform hydrophilic surface separated by a hydrophobic strip three parameters were investigated that affect the spreading dynamics of the droplet: the width of the hydrophobic strip, the gravity and the wetting property of the hydrophilic surface.

Figure 13 shows the evolution of a hemispherical droplet spanning a hydrophobic strip with width  $\delta_{\text{pho}} = 200 \mu\text{m}$ . The contact angles are set as  $\theta_{\text{phi}} = 20^\circ$ ,  $\theta_{\text{pho}} = 160^\circ$ , respectively. As shown in Fig. 13, the droplet spreading process is similar to that in Figs. 9 and 12 at the early stages. However, spreading on the hydrophilic surfaces is not limited by a second hydrophobic strip and the shape of the front of the contact line advancing on the hydrophilic surface becomes circular. Viewed from top, the drop has a butterfly like shape

located over the hydrophobic strip and the two ‘wings’ are connected by neck that has pulled off the hydrophobic strip to form a bridge. As spreading proceeds, the two wings of the butterfly pattern grow while the bridge neck eventually pinches off at time  $t = 17.6$  ms. Two separate droplets emerge after breakage has occurred. Thereafter, the two isolated droplets continue spreading until equilibrium state is attained.

To further study the spreading dynamics of a droplet on a heterogeneous surface, we define dimensionless spreading area and bridge area as

$$\underline{A}_{\text{spr}} = \frac{A_{\text{spr}}}{A_{\text{spr}}^0}, \quad \underline{A}_{\text{bri}} = \frac{A_{\text{bri}}}{A_{\text{bri}}^0}, \quad (62)$$

where  $A_{\text{spr}}$  and  $A_{\text{bri}}$  are the spreading and bridge area of a droplet, respectively, and  $A_{\text{spr}}^0$  and  $A_{\text{bri}}^0$  are initial values of  $A_{\text{spr}}$  and  $A_{\text{bri}}$ , respectively.

Figure 14 shows the bridge area  $\underline{A}_{\text{bri}}$  and spreading area  $\underline{A}_{\text{spr}}$  as a function of time. For the case of  $\delta_{\text{pho}} = 200 \mu\text{m}$ , in the initial stage, the droplet spreads at a lower speed because only a small region of the liquid is in contact with the hydrophilic surface. At time  $t = 2.0$  ms, the spreading speeds up. Further spreading causes an increase in total interfacial surface area of the drop and, thus, produces an increase in the total interfacial energy; thereby decreasing the instantaneous spreading rate. After the neck breaks up, the spreading rate returns to a higher value and then gradually slows as the equilibrium state is approached.

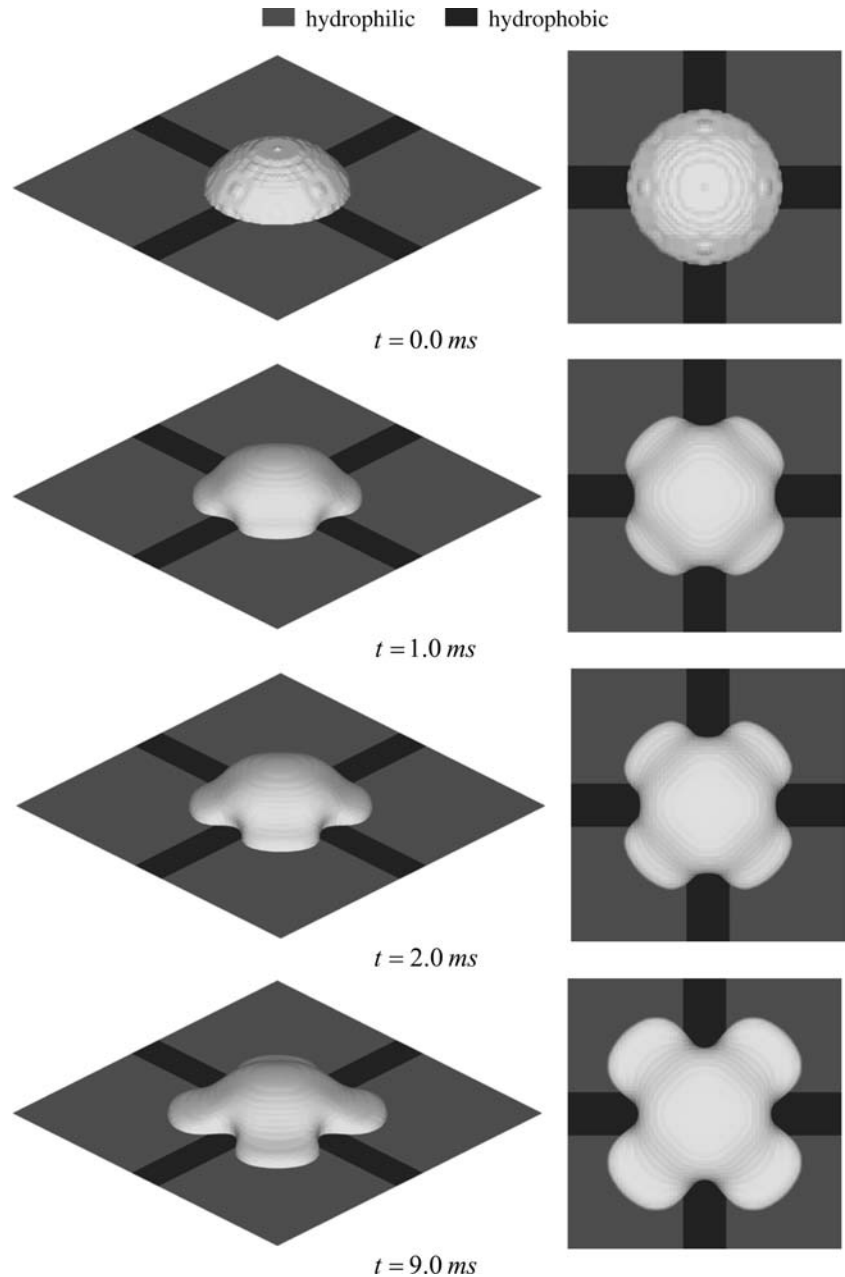
Decreasing the width of the hydrophobic strip reduces the spreading rate and delays the breakup time of the neck, as shown by the curve for  $\delta_{\text{pho}} = 140 \mu\text{m}$  in Fig. 14. However, when the width of the hydrophobic strip is reduced below some critical value, the initial spreading rate is rapid and then slows down to zero, as shown in case  $\delta_{\text{pho}} = 80 \mu\text{m}$  in Fig. 14. This behavior is similar to a droplet spreading on a homogeneous hydrophilic surface. Also, the bridge area approaches a constant value, showing that the neck cannot break up if the hydrophobic strip is too narrow.

At sufficiently large widths, the adhesive force of the hydrophilic surface cannot overcome the repulsive force exerted in the drop by the hydrophobic strip. In this case, the droplet cannot be stretched towards both hydrophilic sides. The final state of the droplet will only contact the hydrophobic strip in a small region. This is shown in the curve of  $\delta_{\text{pho}} = 300 \mu\text{m}$  in Fig. 14, for, which the bridge area increases and the spreading area decreases quickly to a constant value.

The effect of gravity on spreading process is presented in Fig. 15 for fixed wetting properties of the heterogeneous surface  $\theta_{\text{phi}} = 20^\circ$ ,  $\theta_{\text{pho}} = 160^\circ$  and the width of hydrophobic strip  $\delta_{\text{pho}} = 200 \mu\text{m}$ . It is found that gravity increases the spreading rate and accelerates breakup of the droplet neck when the gravity is relatively smaller and vice versa when it is larger.

The wetting properties of the hydrophilic surface also affect droplet spreading behavior. To examine this the

**Fig. 17** Droplet spreading on a heterogeneous surface with intersecting hydrophobic strips. The initial droplet is located on the center of the intersection.  $\delta_{\text{pho}} = 200 \mu\text{m}$ ,  $\theta_{\text{phi}} = 40^\circ$ ,  $\theta_{\text{pho}} = 100^\circ$ ,  $g = 9.8 \text{ m/s}^2$



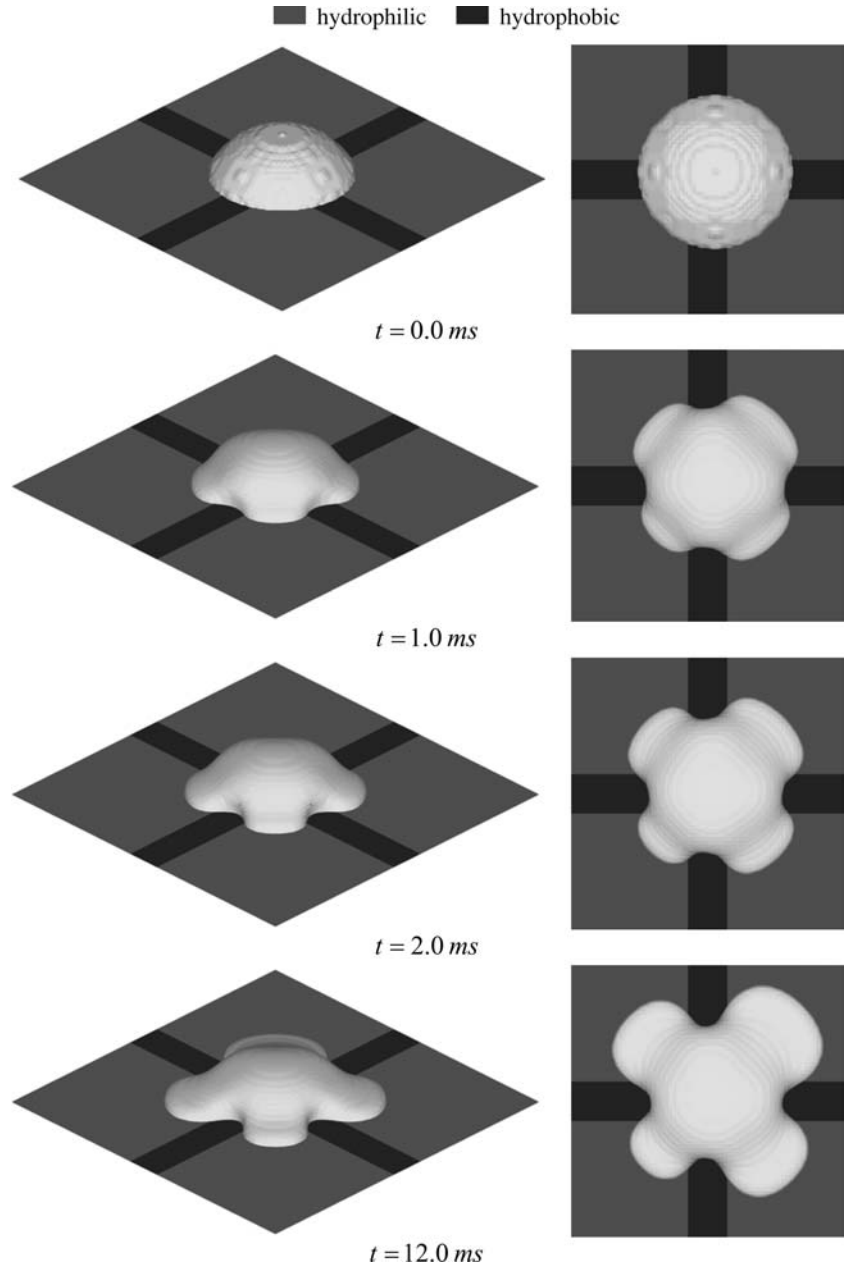
wetting properties of the hydrophilic surfaces were varied while the contact angle and width of the hydrophobic strip were kept constant at  $\theta_{\text{pho}} = 160^\circ$ ,  $\delta_{\text{pho}} = 200 \mu\text{m}$  and gravity is neglected ( $g = 0$ ). The results are shown in Fig. 16. Clearly, an increased contact angle  $\theta_{\text{phi}}$  reduces spreading rate and delays neck breakup. When the contact angle is too large,  $\theta_{\text{phi}} = 60^\circ$ , the wetting forces exerted by the hydrophilic strip on the droplet are not large enough to stretch the bridge to a point at which it breaks.

### 3.6 Droplet spreading on heterogeneous surface with intersecting hydrophobic strips

Finally, droplet spreading on a heterogeneous surface with intersecting hydrophobic strips was investigated.

The surface is a uniform hydrophilic substrate ( $\theta_{\text{phi}} = 40^\circ$ ) with two intersecting hydrophobic strips ( $\theta_{\text{pho}} = 100^\circ$ ) each having a width  $\delta_{\text{pho}} = 200 \mu\text{m}$ . The initial droplet has a shape of spherical cap with radius  $r = 400 \mu\text{m}$  and height  $h = 200 \mu\text{m}$  and is located at the center of the intersecting strips. The evolution of the droplet spreading dynamics is shown in Fig. 17. The droplet quickly contracts inward along the hydrophobic intersection and the central height of the droplet increases at the initial stage. It then symmetrically spreads into the four hydrophilic quadrants and the central height of the drop decreases. The final droplet at equilibrium state has a shape reminiscent of a four-leaved clover. If the initial droplet is off-center, symmetric spreading does not occur. In Fig. 18, the initial droplet is located with its center shifted toward the upper right

**Fig. 18** Droplet spreading on a heterogeneous surface with intersecting hydrophobic strips. The initial displacements of the center  $(0,0)$  of the droplet from the center of the intersection are  $(40,40)$   $\mu\text{m}$ .  $\delta_{\text{pho}} = 200$   $\mu\text{m}$ ,  $\theta_{\text{phi}} = 40^\circ$ ,  $\theta_{\text{pho}} = 100^\circ$ ,  $g = 9.8$   $\text{m/s}^2$



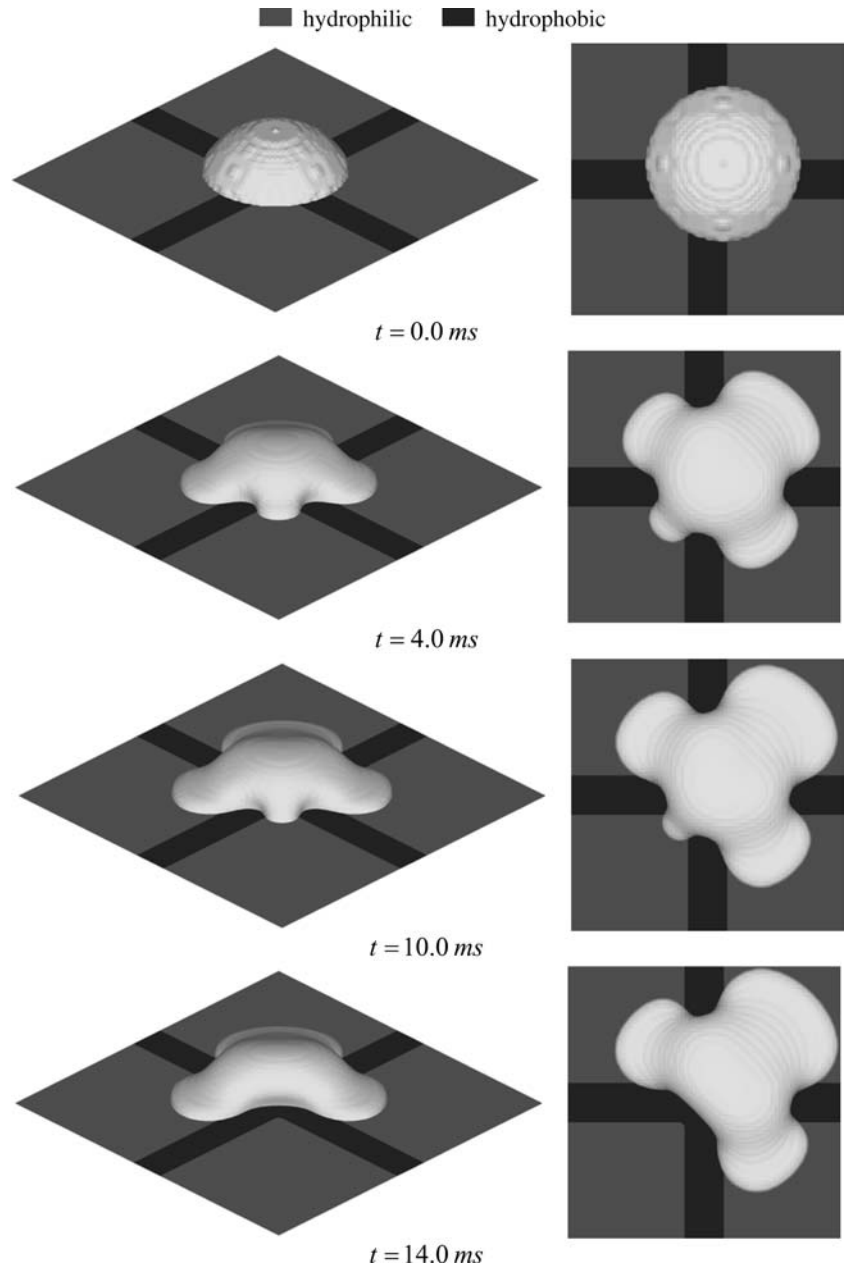
quadrant. The droplet subsequently spreads toward the upper right quadrant faster than in the other quadrants. At time  $t = 12$  ms, it approaches equilibrium. For larger initial off-center displacements as shown in Fig. 19, the branch in the lower left quadrant initially attempts to spread and reaches its maximum extent at time  $t = 4$  ms. Thereafter it starts to shrink and ultimately disappears. Rather than slipping to the hydrophilic region as shown in the results by Dupuis and Yeomans (2005a), the droplet still spans the intersecting hydrophobic strips at the final spreading stage, because the diameter of the droplet is relative bigger to the hydrophobic strips and the initial location of the droplet is close to the center of the intersecting hydrophobic strips.

#### 4 Conclusions

In this work the lattice Boltzmann method (LBM) is used to study droplet spreading on a heterogeneous surface. An adhesive force model was established by nearest-neighbor solid lattice adhesive force with multi-phase LBM. The validation of adhesive force model was verified by comparing with theoretical solution of capillary rise and experimental results of droplet spreading on a heterogeneous surface.

The effect of the initial droplet position on the droplet spreading dynamics was analyzed. As the displacement of the center of the droplet from the centerline of the

**Fig. 19** Droplet spreading on a heterogeneous surface with intersecting hydrophobic strips. The initial displacements of the center  $(0,0)$  of the droplet from the center of the intersection are  $(80,80) \mu\text{m}$ .  $\delta_{\text{pho}} = 200 \mu\text{m}$ ,  $\theta_{\text{phi}} = 40^\circ$ ,  $\theta_{\text{pho}} = 100^\circ$ ,  $g = 9.8 \text{ m/s}^2$



middle hydrophobic strip increases, the droplet shape becomes more asymmetric about the centerline of the middle hydrophobic strip during the spreading process, although the final droplet returns its symmetric about that centerline. If the displacement exceeds a critical value, the droplet only moves toward the nearest hydrophilic strip and then stretches on it.

The droplet spanning a hydrophobic strip may break up if some conditions are satisfied. These conditions include the wettability of hydrophobic and hydrophilic strip, gravity and width of the hydrophobic strip. Increasing the width of the hydrophobic strip and the contact angle of the fluid on the hydrophilic surface all lead to increases in the spreading rate and the tendency of the drop to break up and also reduce the time to break up.

The droplet spreading dynamics on a heterogeneous surface with intersecting hydrophobic strips was also analyzed. A drop spreads symmetrically into all four quadrants when the initial droplet is located at the center of the intersecting strips. If the initial off-center displacement of the droplet relative to the intersecting hydrophobic strips exceeded a critical value, some lobes of the droplet shrink and may eventually disappear.

The results of these simulations demonstrate that the LBM is readily adapted to problems requiring the tracking of sharp interfaces between different phases and can be a useful tool in calculating dynamic equilibrium shapes obtained by varying the system parameters. The analysis of droplet spreading behavior on regularly heterogeneous surface can be readily extended to randomly heterogeneous substrates and to situations where

the fluid properties are functions of temperature (e.g., temperature dependent transport coefficient, viscosity and considerable surface tension variations).

**Acknowledgments** The authors acknowledge support from the National Aeronautics and Space Administration through NASA grant NAG8-1727 and through the National Center for Space Exploration.

## References

- Adão MH, de Ruijter M, Voué M, De Coninck J (1999) Droplet spreading on heterogeneous substrates using molecular dynamics. *J Phys Rev E* 59:746–750
- Bekink S, Karaborni S, Verbist G, Esselink K (1996) Simulating the spreading of a drop in the terraced wetting regime. *Phys Rev Lett* 76:3766–3769
- Bhatnagar PL, Gross EP, Krook M (1954) A model for collision processes in gases, I: small amplitude processes in charged and neutral one component system. *Phys Rev* 94:511–525
- Blake TD (1993) In: Berg JC (ed) Marcel Dekker, Wettability, Chapter 5, NY
- Carnahan NF, Starling KE (1969) Equation of state for nonattracting rigid sphere. *J Chem Phys* 51:635–636
- Cercignani C (1975) Theory and Application of the Boltzmann Equation. Scottish Academic press, Edinburgh
- Chapman S, Cowling TG (1970) The mathematical theory of non-uniform gases. Cambridge University Press, Cambridge, NY
- De Coninck J, de Ruijter MJ, Voué M (2001) Dynamics of wetting, current opinion in colloid interface. *Science* 6:49–53
- De Gennes PG (1985) Wetting: statics and dynamics. *Rev Mod Phys* 57:827–863
- Deng T, Ha S, Cheng JY, Ross CA, Thomas EL (2002) Micropatterning of block copolymer solutions. *Langmuir* 18:6719–6722
- D’Ortona U, De Coninck J, Koplik J, Banavar JR (1996) Terraced spreading mechanisms for chain molecules. *Phys Rev E* 53:562–569
- Dupuis A, Yeomans JM (2004) Lattice Boltzmann modelling of droplets on chemically heterogeneous surfaces. *Future Generation Computer system* 20:993–1001
- Dupuis A, Yeomans JM (2005a) Droplet dynamics on patterned substrates. *Pramana J Phys* 64(6):1019–1027
- Dupuis A, Leopoldes J, Bucknall DG, Yeomans JM (2005b) Control of drop positioning using chemical patterning. *Appl Phys Lett* 87:024103–024103
- Frisch U, d’Humières D, Hasslacher B, Lallemand P, Pomeau Y, Rivet JP (1987) Lattice gas hydrodynamics in two and three dimensions. *Complex Syst* 1:649–707
- Gau H, Herminghaus S, Lenz P, Lipowsky R (1999) Liquid morphologies on structured surfaces: from microchannels to microchips. *Science* 283(5398):46–49
- Grunau D, Chen S, Eggert K (1993) A lattice Boltzmann model for multiphase fluid flows. *Phys Fluids A* 5:2557–2562
- Gunstensen AK, Rothman DH, Zaleski S, Zanetti G (1991) Lattice Boltzmann model of immiscible fluids. *Phys Rev A* 43:4320–4327
- Haataja M, Nieminen JA, Ala-Nissila T (1996) Dynamics of the spreading of chainlike molecules with asymmetric surface interactions. *Phys Rev E* 53:5111–5122
- He X, Doolen G (2002) Thermodynamic foundations of kinetic theory and lattice Boltzmann models for multiphase flows. *J Stat Phys* 107(1/2):309–328
- He X, Luo LS (1997) Theory of the lattice Boltzmann: from the Boltzmann equation to the lattice Boltzmann equation. *Phys Rev E* 56:6811–6817
- He X, Shan X, Doolen GD (1998) Discrete Boltzmann equation model for nonideal gases. *Phys Rev E* 57(1):R13–R16
- He X, Chen S, Zhang R (1999) A lattice Boltzmann scheme for incompressible multiphase flow and its application in simulation of Rayleigh–Taylor instability. *J Comp Phys* 152:642–663
- Lenz P, Lipowsky R (1998) Morphological transitions of wetting layers on structured surfaces. *Phys Rev Lett* 80:1920–1923
- Leopoldes J, Dupuis A, Bucknall DG, Yeomans JM (2003) Jetting micron-scale droplets onto chemically heterogeneous surface. *Langmuir* 19:9818–9822
- Martys NS, Chen H (1996) Simulation of multicomponent fluids in complex three-dimensional geometries by the lattice Boltzmann method. *Phys Rev E* 53:743–750
- Mei R, Shyy W, Yu D, Luo LS (2000) Lattice Boltzmann method for 3-D flows with curved boundary. *J Comp Phys* 161:680–699
- Pasandideh-Fard M, Qiao YM, Chandra S, Mostaghimi J (1996) Capillary effects during droplet impact on a solid surface. *Phys Fluids* 8:650–659
- Pompe T, Fery A, Herminghaus S (1998) Image liquid structures on inhomogeneous surfaces by scanning force microscopy. *Langmuir* 14:2585–2588
- Rothman DH, Zaleski S (1994) Lattice-gas models of phase separation: interface, phase transitions and multiphase flow. *Rev Mod Phys* 66:1417–1479
- de Ruijter MJ, Blake TD, De Coninck J (1999) Dynamic wetting studies by molecular modeling simulations of droplet spreading. *Langmuir* 15:7836–7847
- Shan X, Chen H (1993) Lattice Boltzmann model for simulating flows with multiple phases and components. *Phys Rev E* 47:1815–1819
- Shan X, Chen H (1994) Simulation of nonideal gases and liquid-gas phase transitions by the lattice Boltzmann equation. *Phys Rev E* 49:2941–2948
- Sterling JD, Chen S (1996) Stability analysis of lattice Boltzmann methods. *J Comp Phys* 23:196–206
- Succi S (2001) The lattice Boltzmann equation for fluid dynamics and beyond. Clarendon, NY
- Swift MR, Osborn WR, Yeomans JM (1995) Lattice Boltzmann simulation of non-ideal fluids. *Phys Rev Lett* 75:830–833
- Swift MR, Orlandini E, Osborn WR, Yeomans JM (1996) Lattice Boltzmann simulations of liquid-gas and binary fluid systems. *Phys Rev E* 54:5041–5052
- Trevino C, Mendez F, Ferro-Fontan C (1998) Influence of the aspect ratio of a drop in the spreading process over a horizontal surface. *Phys Rev E* 58:4473–4477
- Zosel A (1993) Studies of the wetting kinetics of liquid drops on solid surface. *Colloid Polym Sci* 271:680–687